Physics in Medicine &
Biology

IPEM
Institute of Physics and Engineering in Medicine

ACCEPTED MANUSCRIPT

Secondary neutron spectra and ambient dose equivalent measurements with an extended range Bonner sphere spectrometer in clinical pencil beam scanning using protons, helium, carbon, and oxygen ions

To cite this article before publication: Sebastian Trinkl *et al* 2025 *Phys. Med. Biol.* in press https://doi.org/10.1088/1361-6560/ae281a

Secondary neutron spectra and ambient dose equivalent measurements with an extended range Bonner Sphere Spectrometer in clinical pencil beam scanning using protons, helium, carbon, and oxygen ions

S. Trinkl[1†,2†*] T. Tessonnier[3,4,5†,*,+], V. Mares[1†], M. Dommert[1†,7], M. Wielunski[1], J. J. Wilkens[2,6], K. Parodi[5], W. Rühm[1†,7]

[1] Institute of Radiation Protection, Helmholtz Zentrum München (HMGU), Neuherberg, Germany
[2] Technical University of Munich, TUM School of Natural Sciences, Physics Department, Garching, Germany
[3] Heidelberg Ion Beam Therapy Center, University Hospital Heidelberg, Heidelberg, Germany
[4] Department of Radiation Oncology, University Hospital Heidelberg, Heidelberg, Germany
[5] Department of Medical Physics, Ludwig-Maximilians-Universität München, Garching b. München, Germany
[6] Technical University of Munich, TUM School of Medicine and Health, Department of Radiation Oncology, TUM University Hospital, Munich, Germany
[7] Federal Office for Radiation Protection, Oberschleißheim, Germany

[*] S.Trinkl and T.Tessonnier contributed equally to this work.
[†] Institution at the time of the study
[+] Corresponding author: thomas.tessonnier@med.uni-heidelberg.de

Abstract.

Objectives: Particle therapy is an advanced radiotherapy technique primarily using protons and carbon ions, with helium and oxygen ions also being considered for clinical applications. A critical concern in ion therapy is the production of secondary neutrons due to nuclear reactions, which may contribute to unwanted dose deposition within the patient.

Approach: This study investigates neutron production for different ion species and energies, providing essential data for assessing secondary neutron exposure. Protons, helium, carbon, and oxygen ions were used to irradiate a PMMA phantom at two energies, corresponding to penetration depths of approximately 5 cm and 14 cm in water. The secondary neutron fluence and ambient dose equivalent ($H^*(10)$) were measured using an extended-range Bonner sphere spectrometer at four angular positions (0°, 45°, 90°, and 135°) relative to the beam direction.

Main results: Results showed significant differences in neutron production depending on ion species and energy. The neutron ambient dose equivalent per primary ion in the beam direction varied by a factor of about 50 across the different ion species. When normalized to the absorbed dose in the pristine Bragg peak, variations of up to a factor of 10 were observed between proton and oxygen ions. However, at off-axis positions, neutron ambient dose equivalent per absorbed dose was relatively similar across ion species, even lower for ions heavier than protons when normalizing to the biologically effective treatment dose.

Significance: This study presents the first measurement-based comparative analysis of fluence energy distributions and neutron equivalent doses for protons, helium, carbon, and oxygen ions in a synchrotron-based clinical facility for monoenergetic beams. These findings are highly relevant for evaluating secondary neutron exposure in particle therapy and optimizing treatment strategies to reduce long term-risks of radiation induced second cancers.

1. Introduction

Modern ion beam radiation therapy using pencil beam scanning (PBS) offers more precise dose delivery to tumors than conventional therapy modalities while sparing surrounding healthy tissue [1–4]. Most particle therapy centers can deliver proton beams, but only a few facilities worldwide offer treatment with heavier ions [4,5]. At the Heidelberg Ion-Beam Therapy Center (HIT), four different ion species (protons, helium, carbon, and oxygen ions) can be delivered, with protons, carbon ions, and, more recently, helium ions being used in clinical practice, while oxygen ions being employed exclusively for experimental purposes [6,7]. Each ion species has its own advantages and disadvantages. Protons are lighter than other ion types and, as a result, undergo stronger beam broadening due to elastic scattering and range straggling, leading to a larger spot size and a less favorable lateral/distal dose gradient. In contrast, heavier ions experience fragmentation, which results in unwanted dose deposition beyond the Bragg peak, forming a fragmentation tail [4]. Compared to photons, ions have a higher ionization density, especially in the Bragg peak region, which increases with ion charge and leads to a higher relative biological effectiveness (RBE) [8,9]. This implies that, to achieve a similar biological effect, a lower absorbed dose is required for oxygen ions compared to carbon, helium, or protons.

Recent advancements in radiotherapy have significantly increased the long-term survival rates of cancer patients. However, this improvement also raises concerns about the long-term risks associated with second primary cancers caused by unwanted exposure to scattered and secondary radiation [10–12]. This issue is particularly relevant for pediatric and young adult patients, who may have a long-life expectancy after treatment and, therefore, an extended period during which second primary malignancies could develop [13]. In this context, the advantages and disadvantages of conventional radiotherapy versus ion beam therapy are widely discussed, with the production of secondary radiation, primarily secondary neutrons in particle therapy, being of particular concern [14–19].

Moreover, patients who have been successfully treated form an essential cohort for future epidemiological studies assessing the risk of second primary cancer following radiotherapy. Consequently, precise data on all sources of radiation exposure, including doses from medical imaging, therapeutic doses to the target volume, and doses from secondary radiation at the periphery and beyond the target volume, are indispensable.

The production of secondary neutrons in nucleus-nucleus interactions depends on several factors, such as projectile energy, the number of nucleons in both the projectile and the target nucleus, and various irradiation parameters, including beam angles and beam modifiers [20,21]. As part of ongoing efforts to assess neutron exposure in proton therapy, Working Group 9 of the European Radiation Dosimetry Group (EURADOS)

conducted comprehensive studies to quantify neutron spectra and ambient dose equivalent in particle therapy [22–24].

Along these lines, the present study investigates the production of secondary neutrons in a PMMA phantom irradiated with four different ion beams (protons, helium, carbon, and oxygen ions). Neutron fluence energy distributions and corresponding ambient dose equivalent ($H^*(10)$) values were measured at four locations within an experimental room at HIT, for two beam energies corresponding to penetration depths of approximately 5 cm and 14 cm in water. Such information are indispensable reference data for benchmarking Monte Carlo code that can be used to estimate organ- and patient-specific neutron doses, thereby linking experimental data with patient risk assessment. This study presents the first comprehensive measurement of neutron fluence energy distributions at HIT for all four ion types and two energy levels.

2. Materials and Methods

2.1. Irradiation plans

The experiment was conducted in Q3 2015 at the HIT synchrotron-based facility, which accelerates ions up to 430 MeV/u and delivers them using PBS with beam currents in the range of 0.1–0.5 nA. Two irradiation scenarios were designed for each of the four HIT ion species, utilizing two different beam energies delivered to a 30 × 30 × 30 cm^3 PMMA phantom. A 11 × 11 cm^2 square field was planned at isocenter with a spot step size of 5 mm, resulting in a total of 529 beam spot positions. For protons, the selected beam energies were 74.7 and 139.3 MeV/u, corresponding to water-equivalent ranges of 4.8 cm and 14.1 cm, respectively. Helium ions were delivered at 76.3 and 140.1 MeV/u (ranges of approximately 5.0 cm and 14.2 cm), carbon ions at 138.7 and 263.8 MeV/u (ranges of about 4.7 cm and 14.0 cm), and oxygen ions at 162.9 and 312.6 MeV/u (ranges of approximately 4.7 cm and 13.9 cm). This information is summarized in Table 1. The number of particles required to achieve a maximum Bragg peak absorbed dose of 2 Gy for the low-energy beams and 4 Gy for the high-energy beams was estimated using the FLUKA Monte Carlo code [25–27]. This information was used to normalize the neutron distributions, either per primary particle or per maximum Bragg peak physical absorbed dose.

In addition, in particle therapy, the prescribed dose is weighted by the RBE. While RBE is fixed to 1.1 for protons, the RBE values for the other ions are higher and variable depending on e.g. dose, linear energy transfer, tissue-type. To normalized the value per treatment dose (Gy (RBE)), estimated RBE values of 1.1, 1.7, 2,7 and 3.5 were assumed for protons, helium, carbon and oxygen ions respectively [28].

Ion	Energy (MeV/u)	Range (cm)	Energy (MeV/u)	Range (cm)
p	74.7	4.8	139.3	14.1
He	76.3	4.0	140.1	14.2
C	138.7	4.7	263.8	14.0
O	162.9	4.7	312.6	13.9

Table 1: Selected beam energies and the corresponding water-equivalent ranges for protons (p) and helium (He), carbon (C) and oxygen (O) ions.

2.2. Experimental Setup

Figure 1 shows a photograph of the experimental setup along with a schematic representation of the geometry used for all irradiations. The 30 × 30 × 30 cm^3 PMMA phantom was positioned at the room isocenter, approximately 1.0 m from the beam nozzle exit.

Four measurement positions were defined around the phantom: position 1 was located at 0° relative to the beam direction at a distance of 1.5 m from the phantom center, while positions 2 (45°), 3 (90°), and 4 (135°) were each positioned at a distance of 2.0 m. The experimental room at HIT measures 7.7 × 6.5 × 3.55 m^3, with concrete walls. On the wall opposite the nozzle, an iron shielding structure (2.0 × 2.0 m^2) is integrated in the wall and contains a 50 × 50 × 55 cm^3 opening, within which a water phantom is placed to serve as a beam dump.

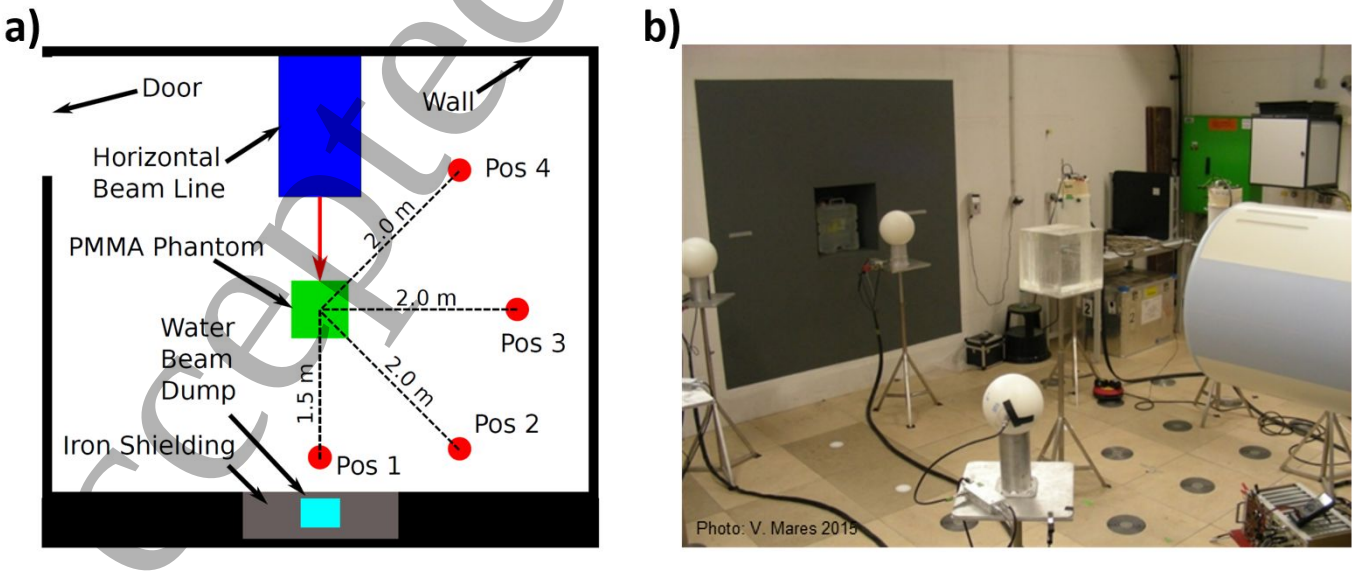

Figure 1: a) Sketch of the setup in the HIT experimental room (not drawn to scale) with the PMMA phantom at isocenter and detectors at position 1 (1.5m, 0°), position 2 (2.0m, 45°), position 3 (2.0m, 90°), and position 4 (2.0m, 135°); b)Photograph of the setup

2.3. Extended-Range Bonner Sphere Spectrometer

Neutron measurements were conducted using an extended-range Bonner sphere spectrometer from Helmholtz Zentrum Munich (HMGU-ERBSS) [22,29]. The HMGU-ERBSS has been utilized in various neutron fields, including secondary neutrons from cosmic rays and proton therapy, with results compared against those obtained using other commonly employed extended-range Bonner sphere spectrometers (ERBSS) [22,29–32].

The HMGU-ERBSS comprises 18 measurement channels, each consisting of a combination of a ^{3}He proportional counter, primarily sensitive to thermal neutrons, and a moderator sphere, which modifies the neutron response function for each channel. Specifically, the system includes 15 pure polyethylene (PE) spheres of varying diameters (2.5, 3, 3.5, 4, 4.5, 5, 5.5, 6, 7, 8, 9, 10, 11, 12, and 15 inches). Additionally, two 9-inch PE spheres contain lead layers of different thicknesses (0.5 and 1 inch) to enhance sensitivity to high-energy neutrons above 20 MeV. One measurement channel consists of a bare ^{3}He proportional counter without a moderator sphere. The ^{3}He proportional counters (Centronics SP9) have a spherical detector volume with a 3.3 cm diameter, filled with ^{3}He gas at a partial pressure of 172 kPa. These 18 detectors were used at the measurement positions shown in Figure 1. The electronic measurement system included a charge-sensitive preamplifier (ARCHEM7E, Canberra Industries Inc.) and a multi-channel analyzer (Multiport II, Canberra Industries Inc.). The Multiport II operated as a fixed dead-time multi-channel analyzer with an overall electronic dead time of less than 18 µs. To minimize dead-time effects, the beam current was adjusted to maintain neutron count rates below 500 counts per second in all spheres under all irradiation conditions. Irradiation times were between 1 and 5 minutes.

2.4. Unfolding and Monte-Carlo simulations

To derive the secondary neutron energy distribution from the 18 single measurements performed under the same conditions, data unfolding is required [33]. In the case of neutron spectrometry where the neutron energy distributions typically span approximately 13 orders of magnitude, or more, with 10 energy bins per decade, unfolding corresponds to a mathematically highly under-determined problem, as only 18 single data points from the different measurement channels are available. In this study the MSANDB unfolding code was used for data processing [34]. MSANDB is an iterative unfolding code using a-priori estimate information about the neutron energy distribution as initial input. To avoid unphysical solutions, like negative neutron fluences, MSANDB applies natural logarithms of neutron fluences.

The accuracy of the unfolding results depends heavily on the quality of the response functions for each measurement channel. These HMGU-ERBSS response functions, including that of the bare ^{3}He proportional counter, were calculated using the Monte

Carlo particle transport code MCNPX including the Los Alamos High Energy Library (LA150) [35]. These response functions were validated up to 384 MeV in quasi-monoenergetic neutron fields at the Osaka Research Center for Nuclear Physics (RCNP) in Japan [36–38].

For each measurement the pulse height distribution of each ^{3}He detector is recorded and the number of ^{3}He(n,p)-reactions that are deduced from this distribution are used in the unfolding procedure. When heavy-ion fragmentation from nuclear reactions produces light charged fragments with ranges exceeding the phantom size, detectors positioned along the beam direction, such as at position 1, may be impacted by these fragments and prompt gamma radiation. Consequently, for the highest-energy heavy-ion beams investigated, the detector at position 1 became saturated in the experiment due to these fragments, especially in the lower channels of the pulse height distribution. As a result, only the measurement results from positions 2, 3, and 4 were analyzed. In contrast, for lower-energy heavy-ion beams, the impact of light fragments on the pulse height distribution at position 1 was minimal. In that case, due to the known ratio of full energy deposition events to partial energy deposition events for each Bonner-sphere, the number of ^{3}He-reactions can be calculated from the full energy deposition peak of the ^{3}He(n,p)-reaction.

A-priori information of the secondary neutron energy distributions required for the MSANDB unfolding code were computed with the Geant4 Monte-Carlo particle transport simulation toolkit [39]. The default physics list QGSP BIC HP was extended to simulate thermal neutrons more precisely inside the PMMA phantom. For this purpose, the G4ThermalNeutronScattering class was included in the G4HadronElasticPhysics class. For hydrogen in PMMA no thermal scattering cross-sections are available. Therefore, the thermal scattering cross-sections for hydrogen in PE were used. Furthermore, to simulate the primary ion beam more accurately the G4StandardElectromagneticPhysics option3 was used instead of the default.

A simple geometry containing only the 30 x 30 x 30 cm^3 PMMA phantom surrounded by dry air together with a rectangular source parallel of 11 x 11 cm^2 was implemented. Phase space files recorded after the HIT beam line, containing both primary and secondary particles, was used to reproduce the experimental beam characteristics and focus for each ion type and energy [40].

Secondary neutron energy distributions were scored at the four measurement positions using 10 cm diameter spheres filled with dry air. A self-implemented G4SensitiveDetector class to score energy distributions, based on the G4ParticleWithEnergy primitive scorer, was implemented, which scores fluence using path length estimation in the scoring volume.

To minimize the large amount of computational time to achieve a-priori secondary neutron energy distributions with a reasonable statistical uncertainty, which was

needed to avoid artificial structures in the unfolded energy distributions for all irradiation conditions, simulation results at 1.0 m distance from the phantom center were used for all measurement positions instead of the real measurement positions. It was initially investigated that the unfolded energy distribution using a-priori information from 1.0 m distance leads to comparable unfolding results (shape and peak heights) as the ones using a-priori information from 1.5 or 2.0 m. Thus, a-priori secondary neutron energy distributions at 1.0 m distance were simulated for each direction, i.e. at 0°, 45°, 90°, and 135° (see Figure 1). Number of histories was about 1.5E9, 1E9, 2E8, 1E8 for protons, helium, carbon and oxygen ions, respectively.

Based on the secondary neutron energy distributions measured with the ERBSS, $H^*(10)$ values were deduced from using fluence-to-ambient dose conversion coefficients. This was done within the MSANDB unfolding code. Contributions to $H^*(10)$ were analyzed for four neutron energy ranges: thermal (1 meV–0.4 eV), epithermal (0.4 eV–100 keV), fast (100 keV–19.4 MeV), and high-energy (≥ 19.6 MeV)[41].

2.5. Estimation of uncertainties in unfolded neutron spectra

Neutron spectrometry with ERBSS is a very complicated method involving various sources of uncertainties and systematic errors. Factors that might contribute to these uncertainties and errors may include choice of unfolding code, simulation of response matrix for a specific ERBSS, calibration of the ERBSS, characteristics of the ERBSS electronics used, primary beam characteristics, stability of beam, geometry of experimental room, space for detector position, distance and angle determination of measurement positions, height of the measurement positions, irradiation time, evaluation of pulse height spectra, choice of simulated a-priori neutron spectra, etc.

While a systematic and overall assessment of the uncertainties and errors was out-of-scope of the present study, it is noted that such an assessment has recently been performed for the energy distributions of secondary neutrons from cosmic radiation. These neutron energy distributions are very similar to those observed behind the shielding of high-energy accelerators, where the secondary neutrons are being produced in the shielding material used [42].

For neutrons from secondary cosmic radiation, uncertainties in total neutron fluence related to the choice of the a-priori neutron distribution were shown to be less than 1% [43], those related to the choice of the unfolding code used were shown to be less than 4% [44], and those related to the choice of the ERBSS response matrix were shown to be less than 5% [45]. Consequently, the overall uncertainty in total neutron fluence was about 7% when error propagation was used.

This is consistent with an overall uncertainty of about 10% in total neutron fluence and ambient dose equivalent based on the neutron fluence energy distribution at the CERF facility at CERN, Switzerland [46].

Consequently, an overall uncertainty of about 10% in Neutron ambient dose equivalent values is estimated in the present study.

3. Results

3.1. Simulation of a-priori secondary neutron energy distributions

Figure 2 shows the simulated a-priori spectra at positions 1 to 4 for the highest protons and lowest carbon ions energies. For both beam energies at position 1 a sharp edge on the right side of the high-energy peak can be seen. This sharp edge is expected due to a maximum energy transfer for a head-on collision between a primary proton hitting a neutron within a nucleus. This is different for the carbon high-energy peak at position 1 (Figure 2b) due to the wide spectrum of possible interactions between a carbon ion and the phantom materials. Consequently, for carbon ions the resulting right side of the high-energy peak shows a smoother edge.

The spectral shapes at positions 2 to 4 are similar for all incident beam energies. Typically, at position 4 a broad peak at about 5-10 MeV can be seen, while at position 3 the peak is at about 10-20 MeV depending on the energy of the primary beam. At all positions and for both ions a small thermal peak is visible. The simulated a-priori neutron energy distributions do not show any evaporation peak, at energies of 1-2 MeV. These evaporation neutrons are typically produced in reactions with high Z-materials because of the increasing probability of evaporation processes in nuclei with many nucleons.

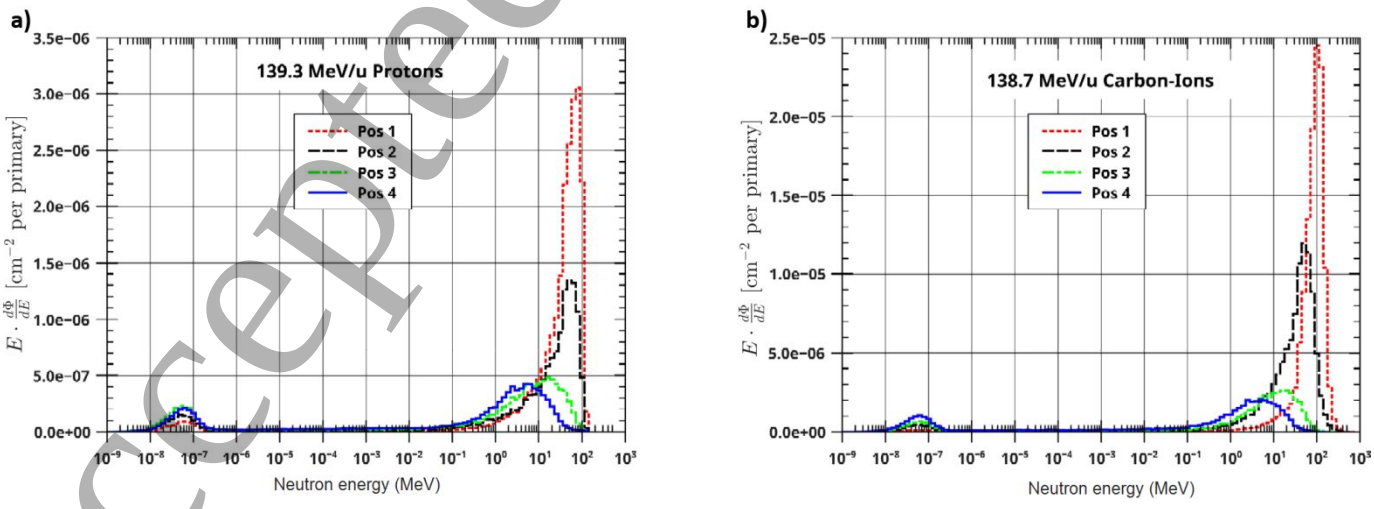

Figure 2: Examples of a-priori secondary neutron energy distributions used for unfolding. a) shows the energy distribution for irradiation with 139.3 MeV/u protons and b) for 138.7MeV/u carbon ions. The energy distributions shown were simulated at a distance of 1.0 m from the phantom center at position 1 (0°), position 2 (45°), position 3 (90°), and position 4 (135°) (see Figure 1).

3.2. Secondary Neutron Fluences

Figures 3 and 4 present the unfolded secondary neutron energy distributions that were based on the ERBSS measurements for the different ions at all positions for the two investigated beam energies, respectively. For the high-energy heavy ions at position 1 secondary neutrons could not be quantified due to saturation of the ^{3}He detectors from light beam fragments, as explained in section 2.4.

At each position the unfolded secondary neutron energy distributions show similar shapes. At position 1 a high-energy peak is visible. In the case of the protons this peak has a sharp edge on the right side, as expected from the a-priori distributions (Figure 2a).

The high-energy peak produced by the 139 MeV/u carbon ions shows a more Gaussian like shape compared to the peak from protons. In contrast to the secondary neutron energy distributions obtained by the Geant4 simulations, those measured with the ERBSS show some evaporation neutrons with a maximum energy around 1-2 MeV.

These neutrons were produced in materials surrounding the measurement positions like concrete walls, the beam dump or additional shielding materials like the iron shielding in beam direction. Due to room layout confidentiality, these structures and materials could not be modeled in the Geant4 simulations.

For the proton, helium and oxygen ions, neutrons in the evaporation region contributed around 40% to the total neutron fluence, while for 139 MeV/u carbon ions those neutrons contributed only around 20 %. Thermal and epithermal neutrons typically contributed around 10-20 % to the total neutron fluence, except for 263 MeV/u carbon ions where the epithermal neutrons contributed around 35 %, at all measured positions.

3.3. Secondary Neutron Doses

The neutron ambient dose equivalent values, deduced from the measured ERBSS neutron energy distributions, are shown in Figure 5 and Figure 6, for the low and high beam energies respectively. The neutron doses are by far dominated by fast and high-energy neutrons.

When normalized to a single primary particle, the neutron ambient dose equivalent $H^*(10)$ was, for instance, approximately 150 times higher for 139 MeV/u carbon ions compared to 74.7 MeV protons at position 1. Conversely, for the higher-energy beams (140 MeV protons and 263 MeV/u carbon ions), a difference of about a factor of 60 was observed at position 2, while for the lower-energy beams, this factor was approximately 30. Detailed tables showing the secondary neutron ambient dose equivalent $H^*(10)$ values, categorized by contributions from different energy regions, are available in the supplementary materials.

Table 2 summarizes the secondary neutron ambient dose equivalent $H^*(10)$ values for all irradiation conditions, normalized to the Bragg peak absorbed dose (μSv/Gy) and treatment dose (μSv/Gy (RBE)).

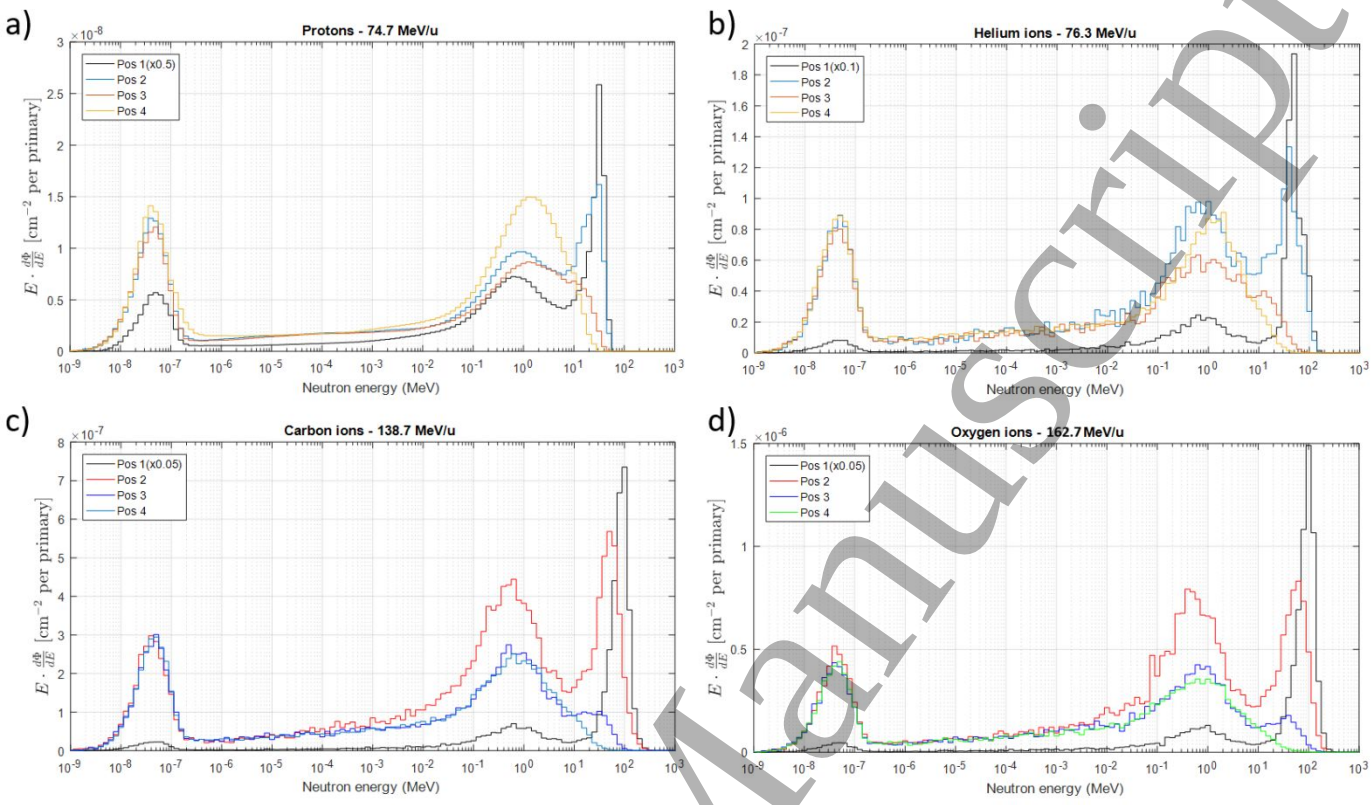

Figure 3: Unfolded secondary neutron energy distributions using the MSANDB unfolding code with 500 iterations, normalized per primary particle for irradiations at the different measurement positions with a) 74.7 MeV/u protons, b) 76.3 MeV/u helium ions, c) 138.7 MeV/u carbon ions, d) 162.9 MeV/u oxygen ions, for a penetration depth of ca. 5 cm. Scaling factors are used for position 1 for visualization purposes. Uncertainties in $H^*(10)$ values deduced from these distributions are about 10%.

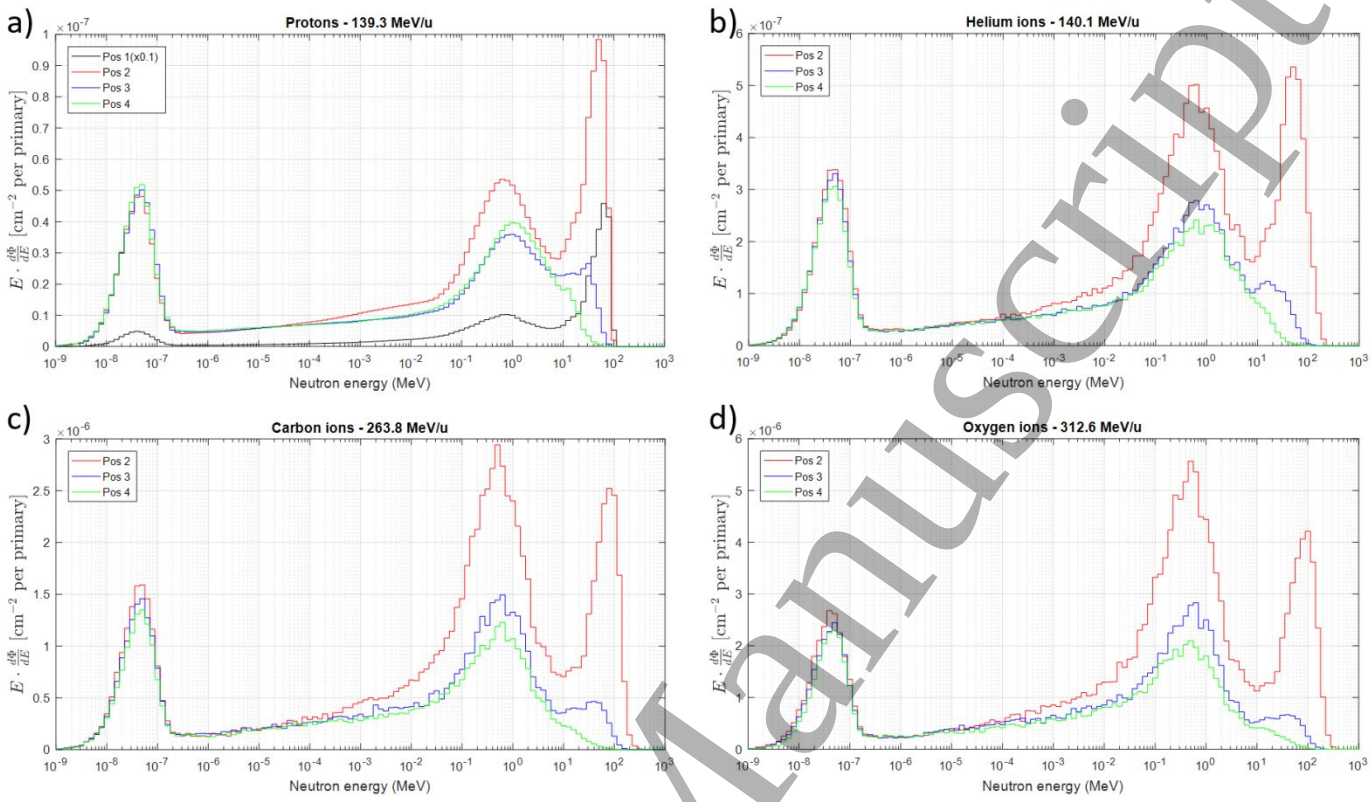

Figure 4: Unfolded secondary neutron energy distributions using the MSANDB unfolding code with 500 iterations, normalized per primary particle for irradiations at the different measurement positions, with a) 139.3 MeV/u protons, b) 140.1 MeV/u helium ions, c) 263.8 MeV/u carbon ions, d) 312.6 MeV/u oxygen ions, for a penetration depth of ca. 14 cm. A scaling factor of 0.1 is used for position 1 for visualization purposes. Uncertainties in $H^*(10)$ values deduced from these distributions are about 10%.

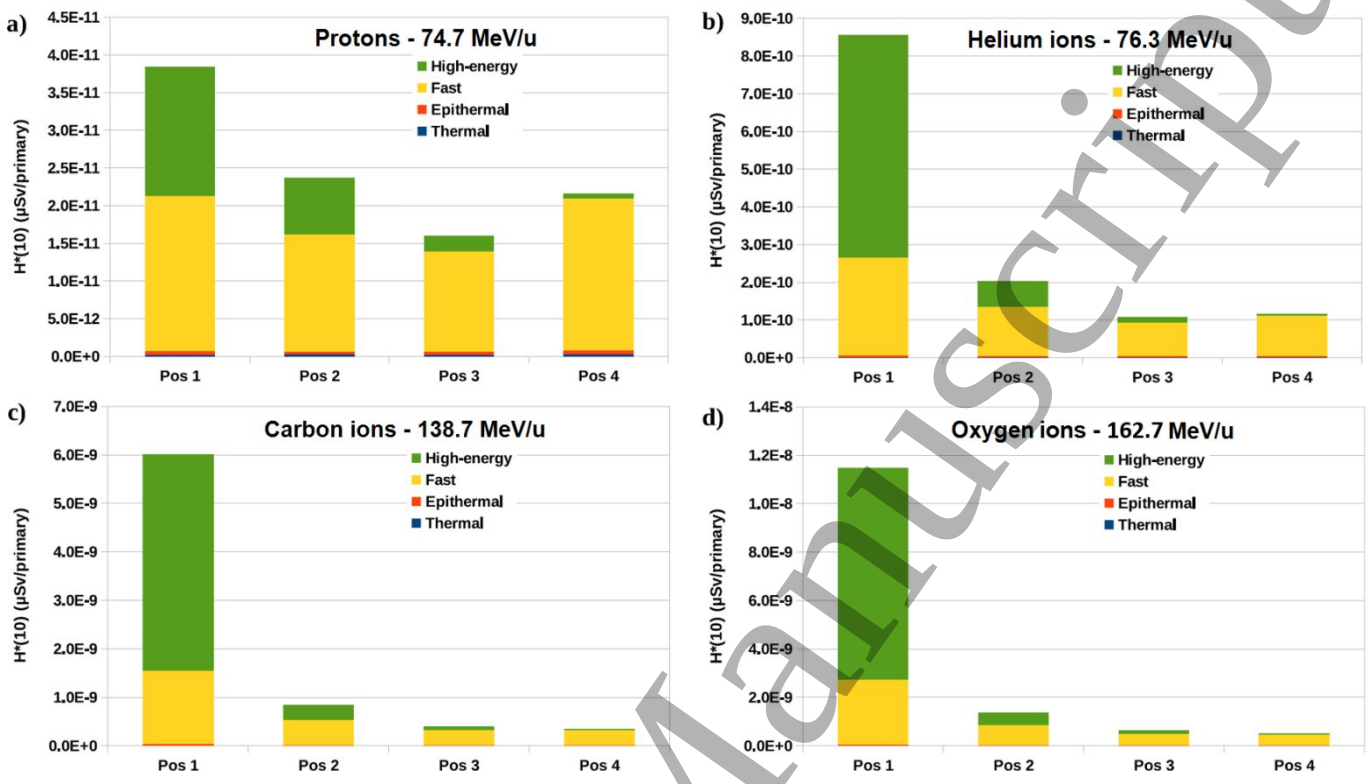

Figure 5: Neutron ambient dose equivalent values $H^*(10)$ normalized per primary particle at the four measurement positions, for different neutron energy regions (high-energy, fast, epithermal, thermal), for irradiations with a penetration depth of c.a. 5cm and an initial beam energies of a) 74.7 MeV/u for protons, b) 76.3 MeV/u for helium ions, c) 138.7 MeV/u for carbon ions and d) 162.9 MeV/u for oxygen ions. Uncertainties in $H^*(10)$ values are about 10%.

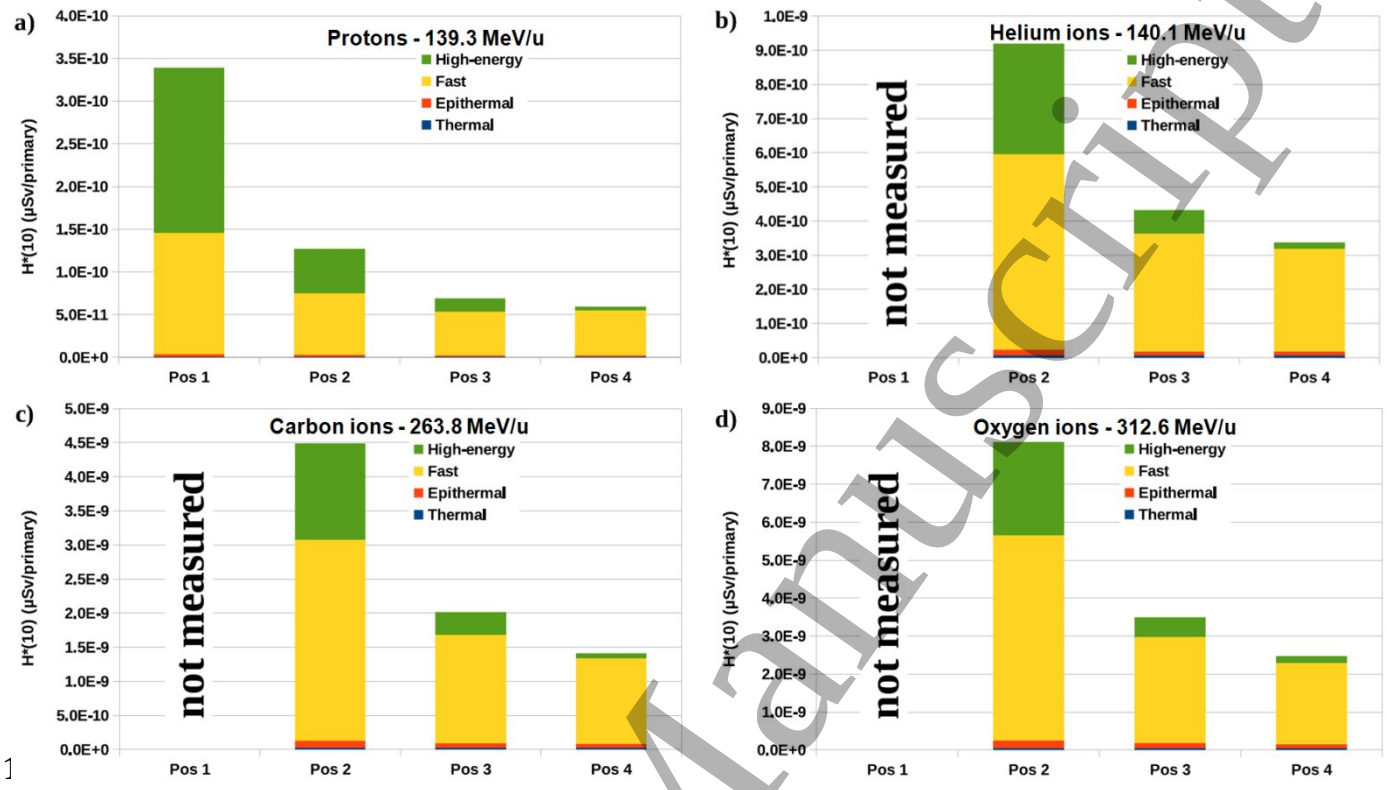

Figure 6: Neutron ambient dose equivalent values $H^*(10)$ normalized per primary particle, for different neutron energy regions (high-energy, fast, epithermal, thermal), for irradiations with a penetration depth of c.a. 14 cm and an initial beam energy of a) 139.3 MeV/u for protons, b) 140.1 MeV/u for helium ions, c) 263.8 MeV/u for carbon ions and d) 312.6 MeV/u for oxygen ions. Uncertainties in $H^*(10)$ values are about 10%.

Particle	Beam energy (MeV/u)	Position / Angle	Distance (m)	$H^*(10)$ per absorbed dose (μSv/Gy)	$H^*(10)$ per treatment dose (μSv/Gy (RBE))
Proton	74.7	1 / 0°	1.5	0.65	0.59
		2 / 45°	2.0	0.40	0.36
		3 / 90°	2.0	0.27	0.25
		4 / 135°	2.0	0.37	0.34
Helium	76.3	1 / 0°	1.5	3.7	2.2
		2 / 45°	2.0	0.85	0.50
		3 / 90°	2.0	0.47	0.28
		4 / 135°	2.0	0.51	0.30
Carbon	138.7	1 / 0°	1.5	5.0	1.9
		2 / 45°	2.0	0.70	0.26
		3 / 90°	2.0	0.33	0.12
		4 / 135°	2.0	0.28	0.10
Oxygen	162.9	1 / 0°	1.5	5.0	1.4
		2 / 45°	2.0	0.63	0.18
		3 / 90°	2.0	0.28	0.08
		4 / 135°	2.0	0.23	0.07
Proton	139.3	1 / 0°	1.5	9.5	8.6
		2 / 45°	2.0	3.6	3.3
		3 / 90°	2.0	1.9	1.7
		4 / 135°	2.0	1.7	1.5
Helium	140.1	1 / 0°	1.5	-	-
		2 / 45°	2.0	6.4	3.8
		3 / 90°	2.0	3.0	1.8
		4 / 135°	2.0	2.4	1.4
Carbon	263.8	1 / 0°	1.5	-	-
		2 / 45°	2.0	5.8	2.1
		3 / 90°	2.0	2.6	1.0
		4 / 135°	2.0	1.8	0.7
Oxygen	312.6	1 / 0°	1.5	-	-
		2 / 45°	2.0	6.9	2.0
		3 / 90°	2.0	3.0	0.9
		4 / 135°	2.0	2.1	0.6

Table 2: Neutron ambient dose equivalent values for all particles and initial beam energies normalized per absorbed dose (Gy) or treatment dose (Gy (RBE)). Uncertainties in $H^*(10)$ values are about 10%.

4. Discussion

This study presents measured neutron fluence energy distributions and corresponding ambient dose equivalents in a clinical setting for proton, helium, carbon, and oxygen ion beams. The results indicate that high-energy neutrons contribute significantly to the total ambient dose equivalent, particularly in the forward direction (position 1, 0 degrees). For example, for protons, high-energy neutrons account for approximately 44% of the total ambient dose equivalent at 74.7 MeV/u initial beam energy, increasing to around 57% for 139.3 MeV/u. This contribution decreases progressively with angle, reaching 3% and 6% at position 4 (135 degrees) for 74.7 and 139.3 MeV/u, respectively. In contrast, at position 4 evaporation neutrons become the dominant contributors, making up 94% and 89% of the total ambient dose equivalent for 74.7 and 139.3 MeV/u, respectively. A similar trend is observed for the other ion species, with high-energy neutron contributions ranging from approximately 75% at position 1 to around 3% at position 4 for the lowest beam energies, with comparable values at higher energies.

When comparing the production of secondary neutrons between protons and heavier ions with similar ranges in the forward direction at the lowest beam energies, helium ions generate approximately 20 times more neutrons per primary ion than protons. This factor increases to about 150 for carbon ions and 300 for oxygen ions due to the greater fragmentation associated with heavier nuclei. At other angles and for both initial beam energies, the neutron production ratio relative to protons is approximately 7 for helium, 30 for carbon, and 50 for oxygen ions. This difference is likely attributed to the higher energy per nucleon required for carbon ions to reach the same depth in the phantom and the larger number of neutrons present in the carbon nucleus compared to protons.

When normalizing by absorbed dose, the differences between ions are significantly reduced, as shown in Table 2. This reduction occurs because less heavier ions are required to achieve the same absorbed dose. Neutron doses from heavier ions remain similar within factors 1 and 2 compared to those from protons, except in the forward direction where they are approximately 6 to 8 times higher. Furthermore, when normalizing with respect to biologically equivalent treatment doses taking the RBE weighting factors into account, neutron doses from heavier ions are either comparable to or lower than those from protons at all measuring positions except in the forward direction, where they remain higher. These findings suggest that while heavy ions, such as carbon ions, were initially assumed to produce significantly higher neutron doses in patients than protons, potentially increasing the risk of second primary malignancies compared to protons, this concern is primarily relevant for organs at risk downstream of the Bragg peak [47–51], that can be the case in cranio-caudal beam orientation for example. In fact, with optimized beam arrangements, treatment plans involving heavier ions could even offer a neutron dose advantage over those involving proton beams.

	Particle	Beam energy (MeV/u)	Angle	Distance (m)	$H^*(10)$ per absorbed dose (µSv/Gy)	$H^*(10)$ per treatment dose (µSv/Gy(RBE))
Trinkl et al.[30]	Proton	75	0°	2.0	0.49	
			45°	2.0	0.39	
			90°	2.0	0.26	
			135°	2.0	0.37	
	Proton	140	0°	2.0	5	
			45°	2.0	3.2	
			90°	2.0	1.6	
			135°	2.0	1.5	
Matsumoto et al. [52]	Carbon	290	90°	2.0		0.6

Table 3: Neutron ambient dose equivalent values for protons and carbons ions from Trinkl et al. [30] and Matsumoto et al. [52], for a single monoenergetic layer, normalized per absorbed dose or treatment dose (Gray / Gray (RBE)).

Neutron spectrometry data in heavy-ion therapy are scarce, with most available data derived from Monte Carlo simulations rather than from direct measurements [20,52–61]. One experimental study investigated secondary neutron energy distributions from a water target irradiated with 200 MeV/u carbon ions, using time-of-flight (TOF) spectrometry to analyze light particle spectra directly behind the Bragg peak. The TOF setup featured a self-made phantom and a measurement distance of 3.05 m [21]. However, the 20 MeV threshold of the TOF technique is relatively high compared for example to evaporation neutron energies, which can make up from approximatively 25 to 93% if neutrons dose. Furthermore, this method only captures neutrons traveling directly from the target while excluding scattered components. Consequently, these results are not directly comparable to those obtained in the present study. Nevertheless, a few studies provide measured neutron ambient dose equivalent values for proton and carbon ion beams, allowing for a more direct comparison, with corresponding results summarized in Table 3 [30,52].

For example, similar neutron measurements using the HMGU-ERBSS were conducted at a proton therapy facility [30], where 75 MeV and 140 MeV protons were studied under

comparable conditions. For carbon ions, neutron energy distributions and equivalent dose assessments have been reported in Japan using a different detection system [52], with measurements conducted for 290 MeV/u carbon ions in a larger target. In general, the equivalent dose per treatment Gy (RBE) aligns well with the present study for both ions, though observed variations could stem from differences in experimental setup (detector type, distance to isocenter, initial beam energy) and room design (e.g., shielding, nozzle configuration), resulting in some differences in neutron back scattering and the RBE values needed for normalization. For the other ions investigated, aside from the Monte Carlo study of [54,55], an experimental study conducted in a larger irradiation field examined neutron ambient dose equivalent contributions using WENDI-II, a neutron rem counter [53,62]. Despite methodological differences, the study reported a similar order of magnitude in the differences between heavier ions, such as carbon and oxygen, compared to helium ions.

A more recent EURADOS campaign to measure ambient dose equivalent was carried out at HIT in 2023 for the four different ions using five different rem counters (WENDI-II [55], LINUS [63], passive LINUS [64], LUPIN [65], and BIOREM [66]) for a spread-out Bragg peak (10x10x10 cm^3) with an energy range close to the highest energy used in this work [24]. The measured range of ambient dose equivalent normalized per primary particles for the different positions were similar to the one measured in the present work as seen in supplementary Table 2, despite the major difference in irradiation settings and in the layout of the HIT experimental room between 2015 and 2023 that could impact the results. Among them the addition of an in-room research MRI occupying approximately one fourth of the room [67].

Given the focus on monoenergetic beams, the results presented in this work can be easily used for validation of neutron-dose simulations (from a Monte Carlo or dedicated engine), that can be then deployed for estimation of any unwanted neutron doses received by radiotherapy patients, especially in similar treatment rooms as at HIT [24,54,55]. This is of particular importance for pediatric patients and potential long-time cancer survivors. In fact, in addition to the concepts of normal tissue complication probability (NTCP) linking dose to risk of toxicities in organs at risks or organ excessive dose associating dose to second primary cancer induction (where neutron doses are typically not considered), the estimated neutron dose and its potential effect on long-term cancer risks could add additional information to select the best individualized treatment approaches, including particle species and beam arrangements [10,68–70]. However, so far, no commercial treatment planning system includes such features. Additionally, validating the in-room neutron field could theoretically enhance pediatric treatment comfort, as has been demonstrated by a study suggesting the dose to parents could be acceptable while remaining in the treatment room during their child's irradiation [71]. In our study, a 11x11cm^2 mono-energetic layer was used; however, to

extrapolate our results to a more clinical target size as used in Bolzonella *et al.* [24] (10×10×10 cm^3 target volume at 15 cm depth in water), an increase of approximately 2.4 times in the number of primary particles, and consequently in $H^*(10)$, would be required. This implies that, for a treatment delivering 60 Gy (RBE) in 30 fractions with protons or helium ions, or a moderately hypofractionated treatment delivering 51 Gy (RBE) in 17 fractions with carbon or oxygen ions, a person standing at 135 degrees and 2 meters from the target center would receive a $H^*(10)$, of approximately 216, 202, 86, or 74 μSv, respectively. These values are comparable to the dose received during one or two round-trip flights between Paris and Tokyo (~50 μSv per flight) [72], suggesting the possibility that even for heavier ions that parents presence near their children during particle therapy could be considered.

5. Outlook

This study provides the first measurement-based comparative analysis of fluence energy distributions and neutron equivalent doses for protons, helium, carbon, and oxygen ions in a synchrotron-based clinical facility for monoenergetic beams of different energy levels. The findings are crucial for validating in-room neutron fields simulated by Monte Carlo methods or dedicated engine, assessing patient dose exposure, and offering to clinicians an insight into neutron exposure variations and potential associated risks, based on beam angulation during treatment or particle species.

6. Acknowledgements

T Tessonnier acknowledges funding from the German Research Foundation at the time of the study (DFG, KFO214).

7. Declaration of generative AI in scientific writing

During preparation of this work the author(s) used ChatGPT-3.5 (OpenAI) in order to find synonyms/antonyms to specific words, spell and grammar check the text, and explore alternative ways of phasing already written sentences to improve article readability. After using this tool/service, the authors(s) reviewed and edited the content as needed and take(s) full responsibility for the content of the publication.

8. References

1. Loeffler, J.S.; Durante, M. Charged Particle Therapy-Optimization, Challenges and Future Directions. *Nat. Rev. Clin. Oncol.* **2013**, *10*, 411–424, doi:10.1038/nrclinonc.2013.79.
2. Schardt, D.; Elsässer, T.; Schulz-Ertner, D. Heavy-Ion Tumor Therapy: Physical and Radiobiological Benefits. *Rev. Mod. Phys.* **2010**, *82*, 383–425, doi:10.1103/RevModPhys.82.383.
3. Durante, M.; Haberer, T. Twenty-Five Years of Carbon Ion Radiotherapy in Europe. *Nucl. Phys. News* **2024**, *34*, 21–24, doi:10.1080/10619127.2024.2410679.
4. Durante, M.; Paganetti, H. Nuclear Physics in Particle Therapy: A Review. *Reports Prog. Phys.* **2016**, *79*, 096702, doi:10.1088/0034-4885/79/9/096702.
5. Durante, M.; Debus, J.; Loeffler, J.S. Physics and Biomedical Challenges of Cancer Therapy with Accelerated Heavy Ions. *Nat. Rev. Phys.* **2021**, *3*, 777–790, doi:10.1038/s42254-021-00368-5.
6. Combs, S.E.; Jäkel, O.; Haberer, T.; Debus, J. Particle Therapy at the Heidelberg Ion Therapy Center (HIT) – Integrated Research-Driven University-Hospital-Based Radiation Oncology Service in Heidelberg, Germany. *Radiother. Oncol.* **2010**, *95*, 41–44, doi:10.1016/J.RADONC.2010.02.016.
7. Jäkel, O.; Kraft, G.; Karger, C.P. The History of Ion Beam Therapy in Germany. *Z. Med. Phys.* **2022**, *32*, 6–22, doi:10.1016/J.ZEMEDI.2021.11.003.
8. Dokic, I.; Mairani, A.; Niklas, M.; Zimmermann, F.; Chaudhri, N.; Krunic, D.; Tessonnier, T.; Ferrari, A.; Parodi, K.; Jäkel, O.; et al. Next Generation Multi-Scale Biophysical Characterization of High Precision Cancer Particle Radiotherapy Using Clinical Proton, Helium-, Carbon- and Oxygen Ion Beams. *Oncotarget* **2016**, *7*, 56676, doi:10.18632/ONCOTARGET.10996.
9. Karger, C.P.; Glowa, C.; Peschke, P.; Kraft-Weyrather, W. The RBE in Ion Beam Radiotherapy: In Vivo Studies and Clinical Application. *Z. Med. Phys.* **2021**, *31*, 105–121, doi:10.1016/j.zemedi.2020.12.001.
10. Vedelago, J.; Schmidt, S.; Stengl, C.; Karger, C.P.; Jäkel, O. Secondary Neutrons in Proton and Light Ion Beam Therapy: A Review of Current Status, Needs and Potential Solutions. *Radiat. Meas.* **2024**, *176*, 107214, doi:10.1016/J.RADMEAS.2024.107214.
11. Christ, S.M.; Ahmadsei, M.; Wilke, L.; Kühnis, A.; Pavic, M.; Tanadini-Lang, S.; Guckenberger, M. Long-Term Cancer Survivors Treated with Multiple Courses of Repeat Radiation Therapy. *Radiat. Oncol.* **2021**, *16*, 208, doi:10.1186/S13014-021-01934-Y.
12. Morton, L.M.; Onel, K.; Curtis, R.E.; Hungate, E.A.; Armstrong, G.T. The Rising Incidence of Second Cancers: Patterns of Occurrence and Identification of Risk Factors for Children and Adults. *Am. Soc. Clin. Oncol. Educ. B.* **2014**, e57–e67, doi:10.14694/edbook_am.2014.34.e57.
13. Facoetti, A.; Barcellini, A.; Valvo, F.; Pullia, M. The Role of Particle Therapy in the Risk of Radio-Induced Second Tumors: A Review of the Literature. *Anticancer Res.* **2019**, *39*, 4613–4617, doi:10.21873/ANTICANRES.13641.
14. Dupere, J.M.; Lucido, J.J.; Breen, W.G.; Mahajan, A.; Stafford, S.L.; Bradley, T.B.; Blackwell, C.R.; Remmes, N.B. Pencil Beam Scanning Proton Therapy for

Pregnant Patients With Brain and Head and Neck Cancers. *Int. J. Radiat. Oncol.* **2024**, *118*, 853–858, doi:10.1016/J.IJROBP.2023.09.040.

15. Brenner, D.J.; Hall, E.J. Secondary Neutrons in Clinical Proton Radiotherapy: A Charged Issue. *Radiother. Oncol.* **2008**, *86*, 165–170, doi:10.1016/J.RADONC.2007.12.003.
16. Newhauser, W.D.; Fontenot, J.D.; Mahajan, A.; Kornguth, D.; Stovall, M.; Zheng, Y.; Taddei, P.J.; Mirkovic, D.; Mohan, R.; Cox, J.D.; et al. The Risk of Developing a Second Cancer after Receiving Craniospinal Proton Irradiation. *Phys. Med. Biol.* **2009**, *54*, 2277–2291, doi:10.1088/0031-9155/54/8/002.
17. Hall, E.J. Intensity-Modulated Radiation Therapy, Protons, and the Risk of Second Cancers. *Int. J. Radiat. Oncol.* **2006**, *65*, 1–7, doi:10.1016/J.IJROBP.2006.01.027.
18. Hälg, R.A.; Besserer, J.; Boschung, M.; Mayer, S.; Lomax, A.J.; Schneider, U. Measurements of the Neutron Dose Equivalent for Various Radiation Qualities, Treatment Machines and Delivery Techniques in Radiation Therapy. *Phys. Med. Biol.* **2014**, *59*, 2457–2468, doi:10.1088/0031-9155/59/10/2457.
19. Newhauser, W.D.; Durante, M. Assessing the Risk of Second Malignancies after Modern Radiotherapy. *Nat. Rev. Cancer* **2011**, *11*, 438–448, doi:10.1038/nrc3069.
20. Kry, S.F.; Bednarz, B.; Howell, R.M.; Dauer, L.; Followill, D.; Klein, E.; Paganetti, H.; Wang, B.; Wuu, C.S.; George Xu, X. AAPM TG 158: Measurement and Calculation of Doses Outside the Treated Volume from External-Beam Radiation Therapy. *Med. Phys.* **2017**, *44*, e391–e429, doi:10.1002/MP.12462.
21. Gunzert-Marx, K.; Iwase, H.; Schardt, D.; Simon, R.S. Secondary Beam Fragments Produced by 200 MeV U−1 12C Ions in Water and Their Dose Contributions in Carbon Ion Radiotherapy. *New J. Phys.* **2008**, *10*, 075003, doi:10.1088/1367-2630/10/7/075003.
22. Farah, J.; Mares, V.; Romero-Expósito, M.; Trinkl, S.; Domingo, C.; Dufek, V.; Klodowska, M.; Kubancak, J.; Knežević; Liszka, M.; et al. Measurement of Stray Radiation within a Scanning Proton Therapy Facility: EURADOS WG9 Intercomparison Exercise of Active Dosimetry Systems. *Med. Phys.* **2015**, *42*, 2572–2584, doi:10.1118/1.4916667.
23. Stolarczyk, L.; Trinkl, S.; Romero-Expósito, M.; Mojzeszek, N.; Ambrozova, I.; Domingo, C.; Davidková, M.; Farah, J.; Kłodowska, M.; Knežević; et al. Dose Distribution of Secondary Radiation in a Water Phantom for a Proton Pencil Beam—EURADOS WG9 Intercomparison Exercise. *Phys. Med. Biol.* **2018**, *63*, 085017, doi:10.1088/1361-6560/AAB469.
24. Bolzonella, M.; Caresana, M.; Cirillo, A.; Martí-Climent, J.M.; Martínez-Francés, E.; Mooshammer, C.; Schmidt, S.; Brons, S.; Silari, M.; Stengl, C.; et al. Out-of-Field Neutron Radiation from Clinical Proton, Helium, Carbon, and Oxygen Ion Beams. *Med. Phys.* **2025**, doi:10.1002/MP.17797.
25. Ferrari, A.; Sala, P.R.; Fassò, A.; Ranft, J. FLUKA : A Multi-Particle Transport Code (Program Version 2005). *Cern-2005-010* **2005**, doi:10.5170/CERN-2005-010.
26. Ballarini, F.; Batkov, K.; Battistoni, G.; Bisogni, M.G.; Böhlen, T.T.; Campanella, M.; Carante, M.P.; Chen, D.; De Gregorio, A.; Degtiarenko, P. V.; et al. The FLUKA Code: Overview and New Developments. *EPJ Nucl. Sci. Technol.* **2024**, *10*, 16, doi:10.1051/EPJN/2024015.

27. Tessonnier, T.; Böhlen, T.T.; Ceruti, F.; Ferrari, A.; Sala, P.; Brons, S.; Haberer, T.; Debus, J.; Parodi, K.; Mairani, A. Dosimetric Verification in Water of a Monte Carlo Treatment Planning Tool for Proton, Helium, Carbon and Oxygen Ion Beams at the Heidelberg Ion Beam Therapy Center. *Phys. Med. Biol.* **2017**, *62*, 6579, doi:10.1088/1361-6560/AA7BE4.
28. Dokic, I.; Mairani, A.; Niklas, M.; Zimmermann, F.; Chaudhri, N.; Krunic, D.; Tessonnier, T.; Ferrari, A.; Parodi, K.; Jäkel, O.; et al. Next Generation Multi-Scale Biophysical Characterization of High Precision Cancer Particle Radiotherapy Using Clinical Proton, Helium-, Carbon- and Oxygen Ion Beams. *Oncotarget* **2016**, *7*, 56676–56689, doi:10.18632/oncotarget.10996.
29. Mares, V.; Romero-Expósito, M.; Farah, J.; Trinkl, S.; Domingo, C.; Dommert, M.; Stolarczyk, L.; Van Ryckeghem, L.; Wielunski, M.; Olko, P.; et al. A Comprehensive Spectrometry Study of a Stray Neutron Radiation Field in Scanning Proton Therapy. *Phys. Med. Biol.* **2016**, *61*, 4127–4140, doi:10.1088/0031-9155/61/11/4127.
30. Trinkl, S.; Mares, V.; Englbrecht, F.S.; Wilkens, J.J.; Wielunski, M.; Parodi, K.; Rühm, W.; Hillbrand, M. Systematic Out-of-Field Secondary Neutron Spectrometry and Dosimetry in Pencil Beam Scanning Proton Therapy. *Med. Phys.* **2017**, *44*, 1912–1920, doi:10.1002/MP.12206.
31. Wiegel, B.; Agosteo, S.; Bedogni, R.; Caresana, M.; Esposito, A.; Fehrenbacher, G.; Ferrarini, M.; Hohmann, E.; Hranitzky, C.; Kasper, A.; et al. Intercomparison of Radiation Protection Devices in a High-Energy Stray Neutron Field, Part II: Bonner Sphere Spectrometry. *Radiat. Meas.* **2009**, *44*, 660–672, doi:10.1016/j.radmeas.2009.03.026.
32. Mares, V.; Trinkl, S.; Iwamoto, Y.; Masuda, A.; Matsumoto, T.; Hagiwara, M.; Satoh, D.; Yashima, H.; Shima, T.; Nakamura, T. Neutron Spectrometry and Dosimetry in 100 and 300 MeV Quasi-Mono-Energetic Neutron Field at RCNP, Osaka University, Japan. In Proceedings of the EPJ Web of Conferences; EDP Sciences, September 25 2017; Vol. 153, p. 08020.
33. Reginatto, M. Overview of Spectral Unfolding Techniques and Uncertainty Estimation. In Proceedings of the Radiation Measurements; Pergamon, December 1 2010; Vol. 45, pp. 1323–1329.
34. Matzke, M. Propagation of Uncertainties in Unfolding Procedures. In Proceedings of the Nuclear Instruments and Methods in Physics Research, Section A: Accelerators, Spectrometers, Detectors and Associated Equipment; North-Holland, January 1 2002; Vol. 476, pp. 230–241.
35. Pelowitz, D.B.; others MCNPX User's Manual Version 2.5. 0. *Los Alamos Natl. Lab.* **2005**, *76*, 473.
36. Mares, V.; Pioch, C.; Ruhm, W.; Iwase, H.; Iwamoto, Y.; Hagiwara, M.; Satoh, D.; Yashima, H.; Itoga, T.; Sato, T.; et al. Neutron Dosimetry in Quasi-Monoenergetic Fields of 244 and 387 MeV. *IEEE Trans. Nucl. Sci.* **2013**, *60*, 299–304, doi:10.1109/TNS.2013.2239312.
37. Mares, V.; Sannikov, A.; Schraube, H. The Response Functions of a 3He-Bonner Spectrometer and Their Experimental Verification in High Energy Neutron Fields. *Proc. Third Spec. Meet. Shield. Asp. Accel. Targets Irradiat. Facil.* **1998**, 237–248.
38. Mares, V.; Schraube, H. High Energy Neutron Spectrometry with Bonner Spheres.

IRPA Reg. Symp. Radiat. Prot. Neighb. Ctries. Cent. Eur. Prague. 8-12 Sept. 1998.

39. Agostinelli, S.; Allison, J.; Amako, K.; Apostolakis, J.; Araujo, H.; Arce, P.; Asai, M.; Axen, D.; Banerjee, S.; Barrand, G.; et al. GEANT4 - A Simulation Toolkit. *Nucl. Instruments Methods Phys. Res. Sect. A Accel. Spectrometers, Detect. Assoc. Equip.* **2003**, *506*, 250–303, doi:10.1016/S0168-9002(03)01368-8.
40. Tessonnier, T.; Marcelos, T.; Mairani, A.; Brons, S.; Parodi, K. Phase Space Generation for Proton and Carbon Ion Beams for External Users' Applications at the Heidelberg Ion Therapy Center. *Front. Oncol.* **2016**, *5*, doi:10.3389/fonc.2015.00297.
41. Englbrecht, F.S.; Trinkl, S.; Mares, V.; Rühm, W.; Wielunski, M.; Wilkens, J.J.; Hillbrand, M.; Parodi, K. A Comprehensive Monte Carlo Study of Out-of-Field Secondary Neutron Spectra in a Scanned-Beam Proton Therapy Gantry Room. *Z. Med. Phys.* **2021**, *31*, 215–228, doi:10.1016/J.ZEMEDI.2021.01.001.
42. Mitaroff, A.; Silari, M. The CERN-EU High-Energy Reference Field (CERF) Facility for Dosimetry at Commercial Flight Altitudes and in Space. *Radiat. Prot. Dosimetry* **2002**, *102*, 7–22, doi:10.1093/OXFORDJOURNALS.RPD.A006075.
43. Simmer, G.; Mares, V.; Weitzenegger, E.; Rühm, W. Iterative Unfolding for Bonner Sphere Spectrometers Using the MSANDB Code – Sensitivity Analysis and Dose Calculation. *Radiat. Meas.* **2010**, *45*, 1–9, doi:10.1016/J.RADMEAS.2009.03.023.
44. Barros, S.; Mares, V.; Bedogni, R.; Reginatto, M.; Esposito, A.; Gonçalves, I.F.; Vaz, P.; Rühm, W. Comparison of Unfolding Codes for Neutron Spectrometry with Bonner Spheres. *Radiat. Prot. Dosimetry* **2014**, *161*, 46–52, doi:10.1093/RPD/NCT353.
45. Pioch, C.; Mares, V.; Rühm, W. Influence of Bonner Sphere Response Functions above 20 MeV on Unfolded Neutron Spectra and Doses. *Radiat. Meas.* **2010**, *45*, 1263–1267, doi:10.1016/J.RADMEAS.2010.05.007.
46. Brall, T.; Dommert, M.; Rühm, W.; Trinkl, S.; Wielunski, M.; Mares, V. Monte Carlo Simulation of the CERN-EU High Energy Reference Field (CERF) Facility. *Radiat. Meas.* **2020**, *133*, 106294, doi:10.1016/J.RADMEAS.2020.106294.
47. Nandy, M. Secondary Radiation in Ion Therapy and Theranostics: A Review. *Front. Phys.* **2021**, *8*, 598257, doi:10.3389/fphy.2020.598257.
48. Mohamad, O.; Tabuchi, T.; Nitta, Y.; Nomoto, A.; Sato, A.; Kasuya, G.; Makishima, H.; Choy, H.; Yamada, S.; Morishima, T.; et al. Risk of Subsequent Primary Cancers after Carbon Ion Radiotherapy, Photon Radiotherapy, or Surgery for Localised Prostate Cancer: A Propensity Score-Weighted, Retrospective, Cohort Study. *Lancet Oncol.* **2019**, *20*, 674–685, doi:10.1016/S1470-2045(18)30931-8.
49. Nitta, Y.; Murata, H.; Okonogi, N.; Murata, K.; Wakatsuki, M.; Karasawa, K.; Kato, S.; Yamada, S.; Nakano, T.; Tsuji, H. Secondary Cancers after Carbon-Ion Radiotherapy and Photon Beam Radiotherapy for Uterine Cervical Cancer: A Comparative Study. *Cancer Med.* **2022**, *11*, 2445–2454, doi:10.1002/cam4.4622.
50. Combs, S.E.; Nikoghosyan, A.; Jaekel, O.; Karger, C.P.; Haberer, T.; Münter, M.W.; Huber, P.E.; Debus, J.; Schulz-Ertner, D. Carbon Ion Radiotherapy for Pediatric Patients and Young Adults Treated for Tumors of the Skull Base. *Cancer* **2009**, *115*, 1348–1355, doi:10.1002/cncr.24153.
51. Yonai, S.; Matsumoto, S. Secondary Neutron Dose in Carbon-Ion Radiotherapy: Investigations in QST–NIRS. *J. Radiat. Prot. Res.* **2021**, *46*, 39–47, doi:10.14407/jrpr.2020.00276.

52. Matsumoto, S.; Yonai, S. Evaluation of Neutron Ambient Dose Equivalent in Carbon-Ion Radiotherapy with Energy Scanning. *Radiat. Prot. Dosimetry* **2020**, *191*, 310–318, doi:10.1093/rpd/ncaa166.
53. Matsumoto, S.; Yonai, S. Evaluation of Neutron Ambient Dose Equivalent in Intensity-Modulated Composite Particle Therapy. *Radiat. Prot. Dosimetry* **2021**, *193*, 90–95, doi:10.1093/rpd/ncab031.
54. Vedelago, J.; Geser, F.A.; Munoz, I.D.; Stabilini, A.; Yukihara, E.G.; Jakel, O. Assessment of Secondary Neutrons in Particle Therapy by Monte Carlo Simulations. *Phys. Med. Biol.* **2022**, *67*, 015008, doi:10.1088/1361-6560/AC431B.
55. Geser, F.A.; Stabilini, A.; Christensen, J.B.; Muñoz, I.D.; Yukihara, E.G.; Jäkel, O.; Vedelago, J. A Monte Carlo Study on the Secondary Neutron Generation by Oxygen Ion Beams for Radiotherapy and Its Comparison to Lighter Ions. *Phys. Med. Biol.* **2024**, *69*, 015027, doi:10.1088/1361-6560/AD0F45.
56. Gioscio, E.; Battistoni, G.; Bochetti, A.; De Simoni, M.; Dong, Y.; Fischetti, M.; Mattei, I.; Mirabelli, R.; Muraro, S.; Patera, V.; et al. Development of a Novel Neutron Tracker for the Characterisation of Secondary Neutrons Emitted in Particle Therapy. *Nucl. Instruments Methods Phys. Res. Sect. A Accel. Spectrometers, Detect. Assoc. Equip.* **2020**, *958*, 162862, doi:10.1016/J.NIMA.2019.162862.
57. Yonai, S.; Kase, Y.; Matsufuji, N.; Kanai, T.; Nishio, T.; Namba, M.; Yamashita, W. Measurement of Absorbed Dose, Quality Factor, and Dose Equivalent in Water Phantom Outside of the Irradiation Field in Passive Carbon-Ion and Proton Radiotherapies. *Med. Phys.* **2010**, *37*, 4046–4055, doi:10.1118/1.3458721.
58. Huang, S.C.; Zhang, H.; Bai, K.; Luo, Y.; Mao, H.J.; Dai, Z.Y. Monte Carlo Study of the Neutron Ambient Dose Equivalent at the Heavy Ion Medical Machine in Wuwei. *Nucl. Sci. Tech.* **2022**, *33*, 1–15, doi:10.1007/s41365-022-01093-z.
59. Mattei, I.; Battistoni, G.; De Simoni, M.; Dong, Y.; Embriaco, A.; Fischetti, M.; Gioscio, E.; Mancini-Terracciano, C.; Marafini, M.; Mirabelli, R.; et al. Charged Particles and Neutron Trackers: Applications to Particle Therapy. *Nucl. Instruments Methods Phys. Res. Sect. A Accel. Spectrometers, Detect. Assoc. Equip.* **2020**, *954*, 161229, doi:10.1016/J.NIMA.2018.09.064.
60. Colson, D.; Pinasti, S.; Matamoros Ortega, A.N.; De Saint-Hubert, M.; Van Hoey, O.; Reniers, B. The Influence of Monte Carlo Radiation Transport Codes and Hadron Physics Models on Stray Neutron Dose Estimations in Proton Therapy: An Extended Intercomparison. *Radiat. Meas.* **2024**, *170*, 107046, doi:10.1016/J.RADMEAS.2023.107046.
61. Yonai, S.; Matsufuji, N.; Kanai, T.; Matsui, Y.; Matsushita, K.; Yamashita, H.; Numano, M.; Sakae, T.; Terunuma, T.; Nishio, T.; et al. Measurement of Neutron Ambient Dose Equivalent in Passive Carbon-Ion and Proton Radiotherapies. *Med. Phys.* **2008**, *35*, 4782–4792, doi:10.1118/1.2989019.
62. Olsher, R.H.; Hsu, H.H.; Beverding, A.; Kleck, J.H.; Casson, W.H.; Vasilik, D.G.; Devine, R.T. WENDI: An Improved Neutron Rem Meter. *Health Phys.* **2000**, *79*, 170–181, doi:10.1097/00004032-200008000-00010.
63. Birattari, C.; Ferrari, A.; Nuccetelli, C.; Pelliccioni, M.; Silari, M. An Extended Range Neutron Rem Counter. *Nucl. Instruments Methods Phys. Res. Sect. A Accel. Spectrometers, Detect. Assoc. Equip.* **1990**, *297*, 250–257, doi:10.1016/0168-

9002(90)91373-J.

64. Agosteo, S.; Caresana, M.; Ferrarini, M.; Silari, M. A Passive Rem Counter Based on CR39 SSNTD Coupled with a Boron Converter. *Radiat. Meas.* **2009**, *44*, 985–987, doi:10.1016/J.RADMEAS.2009.10.053.
65. Caresana, M.; Ferrarini, M.; Manessi, G.P.; Silari, M.; Varoli, V. LUPIN, a New Instrument for Pulsed Neutron Fields. *Nucl. Instruments Methods Phys. Res. Sect. A Accel. Spectrometers, Detect. Assoc. Equip.* **2013**, *712*, 15–26, doi:10.1016/J.NIMA.2013.01.060.
66. Caresana, M.; Denker, A.; Esposito, A.; Ferrarini, M.; Golnik, N.; Hohmann, E.; Leuschner, A.; Luszik-Bhadra, M.; Manessi, G.; Mayer, S.; et al. Intercomparison of Radiation Protection Instrumentation in a Pulsed Neutron Field. *Nucl. Instruments Methods Phys. Res. Sect. A Accel. Spectrometers, Detect. Assoc. Equip.* **2014**, *737*, 203–213, doi:10.1016/J.NIMA.2013.11.073.
67. Klüter, S.; Milewski, K.; Johnen, W.; Brons, S.; Naumann, J.; Dorsch, S.; Beyer, C.; Paul, K.; Dietrich, K.A.; Platt, T.; et al. First Dosimetric Evaluation of Clinical Raster-Scanned Proton, Helium and Carbon Ion Treatment Plan Delivery during Simultaneous Real-Time Magnetic Resonance Imaging. *Phys. Imaging Radiat. Oncol.* **2025**, *33*, 100722, doi:10.1016/J.PHRO.2025.100722.
68. Moteabbed, M.; Yock, T.I.; Paganetti, H. The Risk of Radiation-Induced Second Cancers in the High to Medium Dose Region: A Comparison between Passive and Scanned Proton Therapy, IMRT and VMAT for Pediatric Patients with Brain Tumors. *Phys. Med. Biol.* **2014**, *59*, 2883–2899, doi:10.1088/0031-9155/59/12/2883.
69. Palma, G.; Monti, S.; Conson, M.; Pacelli, R.; Cella, L. Normal Tissue Complication Probability (NTCP) Models for Modern Radiation Therapy. *Semin. Oncol.* **2019**, *46*, 210–218, doi:10.1053/j.seminoncol.2019.07.006.
70. Zacharatou Jarlskog, C.; Paganetti, H. Risk of Developing Second Cancer From Neutron Dose in Proton Therapy as Function of Field Characteristics, Organ, and Patient Age. *Int. J. Radiat. Oncol.* **2008**, *72*, 228–235, doi:10.1016/J.IJROBP.2008.04.069.
71. Mares, V.; Farah, J.; De Saint-Hubert, M.; Domański, S.; Domingo, C.; Dommert, M.; Kłodowska, M.; Krzempek, K.; Kuć, M.; Martínez-Rovira, I.; et al. Neutron Radiation Dose Measurements in a Scanning Proton Therapy Room: Can Parents Remain Near Their Children During Treatment? *Front. Oncol.* **2022**, *12*, 903706, doi:10.3389/fonc.2022.903706.
72. Mares, V.; Yasuda, H. Aviation Route Doses Calculated with EPCARD.Net and JISCARD EX. *Radiat. Meas.* **2010**, *45*, 1553–1556, doi:10.1016/j.radmeas.2010.06.015.